Opto-Electronic
Science

ISSN 2097-0382 CN 51-1800/O4

Generation of structured light beams with polarization variation along arbitrary spatial trajectories using tri-layer metasurfaces

Tong Nan, Huan Zhao, Jinying Guo, Xinke Wang, Hao Tian and Yan Zhang

Citation: Nan T, Zhao H, Guo JY, et al. Generation of structured light beams with polarization variation along arbitrary spatial trajectories using tri-layer metasurfaces. *Opto-Electron Sci* **3**, 230052 (2024).

https://doi.org/10.29026/oes.2024.230052

Received: 28 December 2023; Accepted: 26 February 2024; Published online: 28 May 2024

Related articles

Terahertz metasurface zone plates with arbitrary polarizations to a fixed polarization conversion
Zhen Yue, Jitao Li, Jie Li, Chenglong Zheng, Jingyu Liu, Guocui Wang, Hang Xu, Mingyang Chen, Yating Zhang, Yan Zhang, Jianquan Yao
Opto-Electronic Science 2022 **1**, 210014 doi: 10.29026/oes.2022.210014

High-Q resonant terahertz metasurfaces
Manukumara Manjappa, Yuri Kivshar
Opto-Electronic Advances 2024 **7**, 240043 doi: 10.29026/oea.2024.240043

Highly efficient vectorial field manipulation using a transmitted tri-layer metasurface in the terahertz band
Huan Zhao, Xinke Wang, Shutian Liu, Yan Zhang
Opto-Electronic Advances 2023 **6**, 220012 doi: 10.29026/oea.2023.220012

Ultrahigh performance passive radiative cooling by hybrid polar dielectric metasurface thermal emitters
Yinan Zhang, Yinggang Chen, Tong Wang, Qian Zhu, Min Gu
Opto-Electronic Advances 2024 **7**, 230194 doi: 10.29026/oea.2024.230194

More related article in Opto-Electronic Journals Group website

Opto-Electronic Science

Article
May 2024, Vol. 3, No. 5

DOI: 10.29026/oes.2024.230052

Generation of structured light beams with polarization variation along arbitrary spatial trajectories using tri-layer metasurfaces

Tong Nan[1,2], Huan Zhao[3], Jinying Guo[4,5], Xinke Wang[2], Hao Tian[1] and Yan Zhang[2]*

Conventionally, the spatially structured light beams produced by metasurfaces primarily highlight the polarization modulation of the beams propagating along the optical axis or the beams' spatial transmission trajectory. In particular, along the optical axis, the polarization state is either constant or varies continuously in each output plane. Here, we develop innovative spatially structured light beams with continually changing polarization along any arbitrary spatial transmission trajectories. With tri-layer metallic metasurfaces, the geometric characteristics of each layer structure can be adjusted to modulate the phase and polarization state of the incident terahertz (THz) wave. The beam will converge to the predefined trajectory along several paths to generate a Bessel-like beam with longitudinal polarization changes. We demonstrate the versatility of the approach by designing two THz-band structured light beams with varying polarization states along the spatial helical transmission trajectory. Continuous linear polarization changes and linear polarization to right circular polarization (RCP) and back to linear polarization changes are realized respectively. The experimental results are basically consistent with the simulated results. Our proposal for arbitrary trajectory structured light beams with longitudinally varying polarization offers a practical method for continuously regulating the characteristics of spatial structured light beams with non-axial transmission. This technique has potential uses in optical encryption, particle manipulation, and biomedical imaging.

Keywords: structured light beam; tri-layer metallic metasurface; longitudinal polarization; non-axial transmission

Nan T, Zhao H, Guo JY et al. Generation of structured light beams with polarization variation along arbitrary spatial trajectories using tri-layer metasurfaces. *Opto-Electron Sci* **3**, 230052 (2024).

Introduction

A structured light beam is a unique arrangement of different light field properties in space and time[1,2]. While temporal properties concentrate on the temporal and spectral management of the light field, spatial properties handle the control of the light field's amplitude (intensity), phase (wavefront), and polarization. Many unusual beams, including spiral phase beams, Bessel beams, vector beams, Airy beams, and spatiotemporal beams, can be created by adjusting the spatial or even spatiotemporal

[1]School of Physics, Harbin Institute of Technology, Harbin 150001, China; [2]Beijing Key Laboratory of Metamaterials and Devices, Key Laboratory of Terahertz Optoelectronics, Ministry of Education, Beijing Advanced Innovation Center for Imaging Theory and Technology, Department of Physics, Capital Normal University, Beijing 100048, China; [3]Institute of Microelectronics Chinese Academy of Sciences, Beijing 100029, China; [4]Shanghai Institute of Optics and Fine Mechanics, Chinese Academy of Sciences, Shanghai 201800, China; [5]Center of Materials Science and Optoelectronics Engineering, University of Chinese Academy of Sciences, Beijing 100049, China.

*Correspondence: Y Zhang, E-mail: yzhang@cnu.edu.cn

Received: 28 December 2023; Accepted: 26 February 2024; Published online: 28 May 2024

structure of light waves[3–7]. Structured light beams have several traditional uses. For example, the use of Bessel beams can result in increased depth of field in imaging procedures[8]; the use of vortex beams can increase the number of wireless communication channels, improving the communication systems' ability to transmit information[9]; using vector beams to focus can result in smaller focal spots[10]. Structured light beams have become an important research topic in recent years, with many advances being made in fields like optical communication and data transmission[11,12], optical sensing and measurement[13], optical manipulation and control[14], optical encryption[15], quantum information processing[16,17], and super-resolution imaging[18,19].

Spatial light modulators (SLMs) are commonly employed in conventional techniques to produce spatially structured light beams. For example, arbitrary vector beams can be generated based on SLM and a 4-f system[20]. Furthermore, nondiffracting Bessel beams with a polarization state that changes with propagation distance can be produced by combining SLM with a reflecting geometry[21]. Moreover, oscillating polarized vector beams can be formed by cascading SLMs[22]. Nonetheless, current techniques that employ SLMs to produce spatially structured light beams face a number of challenges, such as a restricted operational bandwidth, elevated expenses, poor diffraction efficiency, and restricted integration potential. The advent of metasurfaces offers a new way to manipulate the optical field and a versatile way to build different spatially structured light beams based on requirements[23–34].

However, traditional metasurfaces that produce structured light beams can only manipulate polarization in the two-dimensional space of the *x*-*y* plane, that is, the polarization distribution remains constant in every output plane throughout the propagation path. Recently, scalar light fields[35,36] and vector light fields[37–40] have been employed by researchers to achieve longitudinally varying polarization behavior using metasurfaces, where the polarization state can change continuously as light propagates. The optical axis has been the primary focus of these longitudinal polarization alterations research. Nonetheless, transmission polarization modulation in three dimensions and self-accelerating transmission are also significant dimensions, in addition to modulation along the optical axis. The achievement of longitudinal continuous variation in non-axis and three-dimensional spatial polarization is a highly relevant topic that warrants further investigation in the context of structured light.

This paper reports the creation of new spatially structured light beams that enable polarization to change longitudinally along a helical path in space through the use of tri-layer metallic metasurfaces. In three-dimensional space, arbitrary trajectory beams can be generated using the Bessel-like accelerated beam creation method. Moreover, the polarization control at each point on the arbitrary trajectory can be realized by controlling the amplitude and phase difference of the orthogonal polarized beams. As shown in Fig. 1, metallic metasurfaces with three layers can be used to separately control the polarization and phase of propagating terahertz (THz) wave. The final realization is the continuous manipulation of 15° linear polarization to 75° linear polarization on the helical transmission trajectory, as well as the continuous manipulation of 15° linear polarization to right circular polarization (RCP) and to 75° linear polarization. Our proposed longitudinally variable polarization arbitrary trajectory structured light beam can expand the range of possible configurations for structured light beam propagation and open up new possibilities for creating customized spatial structured light beams.

Principle and design method

An approach to producing accelerated Bessel beams along any path was initially put forth by Chremmos and Zhao et al.[41,42]. Conical beams have continuous beam profiles at their vertices, and when these beams interfere, an accelerated Bessel beam is produced. A metal C-shaped split-ring antenna was utilized to control the incident THz wave's wavefront phase, directing light onto a predetermined trajectory ($f(z)$, $g(z)$, z) to create an accelerated Bessel beam. According to ref.[42], the phase distribution of the metasurface at vertical point z=0 is as follows:

$$Q\left(x,y\right)=\frac{k}{2}\int_{0}^{z}\left\{\left[f'\left(\zeta\right)\right]^{2}+\left[g'\left(\zeta\right)\right]^{2}-\left(1/\left(kl_{0}\right)\right)^{2}\right\}\mathrm{d}\zeta-k\frac{\left(f-x\right)^{2}+\left(g-y\right)^{2}}{2z}\ , \tag{1}$$

where (x, y) is the two-dimensional coordinate system of the plane on which the metasurface is placed; k is the wave number of free space in vacuum; l_0 is the normalization coefficient of cross section coordinates. The predefined trajectory ($f(z)$, $g(z)$, z) satisfies the following relation:

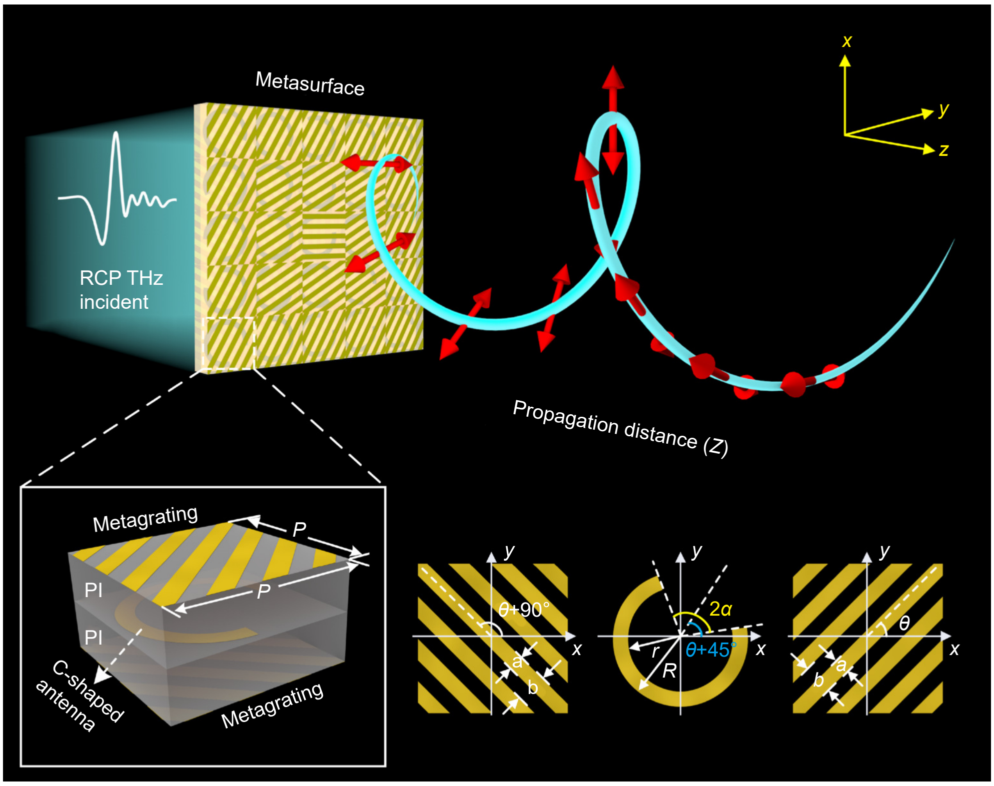

Fig. 1 | Schematic diagram for generation of a structured light beam with polarization variation along arbitrary spatial trajectories using tri-layer metasurface.

$$\frac{z^2}{k^2 l_0^{\,2}} = [x - f(z) + zf'(z)]^2 + [y - g(z) + zg'(z)]^2 \,. \quad (2)$$

The preceding formula shows that the circle's center moves gradually as z increases and that the analogous circles' radii continue to expand. The beam ($f(z)$, $g(z)$, z) transmission trajectory is the vertex of conical light emitted from these constantly moving equivalent circles. When two zero-order Bessel Gaussian beams with orthogonal polarization are superposed, the electric field E can be written as follows:

$$\begin{aligned} \boldsymbol{E}(r,z) =& \exp\left(-\frac{r^2}{\omega_0^2}\right) J_0(k_r r)\exp(\mathrm{i}k_z z) \\ &\cdot \left[E_1(z)\,\mathrm{e}^{\mathrm{i}\delta_1(z)}\boldsymbol{e}_1 + E_2(z)\,\mathrm{e}^{\mathrm{i}\delta_2(z)}\boldsymbol{e}_2\right] \,, \end{aligned} \quad (3)$$

where E_1 and E_2 correspond to the axial amplitude distribution of the two polarization eigenstates, respectively, the axial amplitude ratio and phase difference determine the change in polarization during propagation. To generate the predesigned transmission trajectory and polarization distribution, the design of the metasurface includes two parts: transmission trajectory design and polarization control. Equation (2) reveals that any point on predesigned transmission trajectory is the apex of a conical ray bundle emanating from a circle on the input plane. In addition, the polarization control at each point on the predesigned transmission trajectory can be realized by controlling the amplitude and phase difference of the orthogonal polarized beams corresponding to different circles.

With the use of a tri-layer metallic metasurface (details can be found in the design method), the top and bottom layers act as two polarizers with orthogonal polarization orientations due to their mutually perpendicular metagratings. Meanwhile, the middle layer —which consists of split-ring antennas with metallic C shapes—is used to adjust the phase of transmitted wave. The Jones matrix for the tri-layer metallic metasurface can be represented as[31]:

$$\begin{aligned} \boldsymbol{J} =& \begin{bmatrix} \sin^2\theta & -\sin\theta\cos\theta \\ -\sin\theta\cos\theta & \cos^2\theta \end{bmatrix} \\ &\cdot \begin{bmatrix} 0 & t_{xy}\mathrm{e}^{\mathrm{i}\varphi_{xy}(\alpha)} \\ t_{yx}\mathrm{e}^{\mathrm{i}\varphi_{yx}(\alpha)} & 0 \end{bmatrix} \\ &\cdot \begin{bmatrix} \cos^2\theta & \sin\theta\cos\theta \\ \sin\theta\cos\theta & \sin^2\theta \end{bmatrix} \\ =& t_{xy}\mathrm{e}^{\mathrm{i}\varphi_{xy}(\alpha)} \cdot \begin{bmatrix} -\sin\theta\cos\theta & \cos^2\theta \\ -\sin^2\theta & \sin\theta\cos\theta \end{bmatrix} \,, \end{aligned} \quad (4)$$

where, t_{xy}, t_{yx} and φ_{xy}, φ_{yx} represent the amplitude transmittance and phase for cross-polarization, respectively. α

denotes the opening angle of the metallic C-shaped splitting antennas, while θ represents the angle between the orientation of the bottom layer metagrating and the x-axis, as shown in the bottom of Fig. 1. Incoming THz waves sequentially pass through the metasurface from the lowest layer to the upper layer.

The predefined trajectory is a cylindrical helical path ($f(z)$ = 0.3cos(πz/20), $g(z)$ = 0.3sin(πz/20)). The phase distribution at the input plane is obtained at a specified wavelength of 400 μm based on Eqs. (1) and (2), as illustrated in Fig. 2(a). In order to achieve longitudinal variations in linear polarization shown in Fig. 2(b), we optimized the phase distribution at the input plane into several regions based on Eq. (3). Within these distinct regions, we modulated the amplitude components E_x and E_y to achieve diverse forms of longitudinal polarization modulation. As depicted in Fig. 2(c), the input phase plane was separated into four sections, the orientations of the bottom layer metagratings of the corresponding tri-layer metasurface are 0°, 30°, 60°, and 90°, from inner to outer. As a result, this arrangement led to a gradual decrease in the amplitude component E_x and an increase in E_y from the innermost to the outermost sections. Consequently, this approach enabled the attainment of linear polarization changes along the predefined transmission trajectory. The polarization states corresponding to different propagation distances z are illustrated on the Poincaré sphere, as shown in Fig. 2(d). It is noteworthy

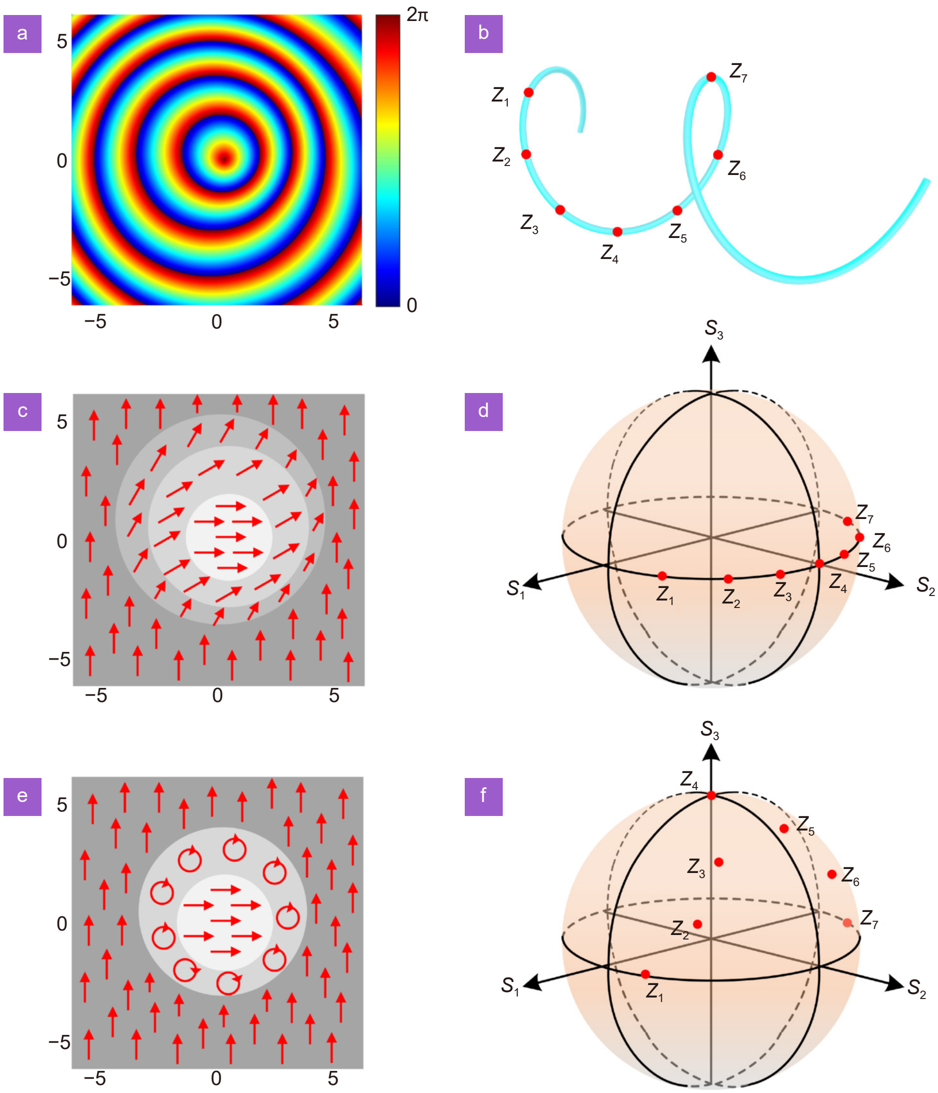

Fig. 2 | Schematic diagram of design concept for structured light beams. (**a**) The phase distribution at the input plane. (**b**) Spatial transmission trajectory of cylindrical helical path. (**c**) Polarization distributions on the input plane. (**d**) The polarization states corresponding to different propagation distances *z* on the Poincaré sphere for linear longitudinal polarization variations. (**e**) Polarization distributions on the input plane. (**f**) The polarization states corresponding to different propagation distances *z* on the Poincaré sphere for nonlinear longitudinal polarization variations.

that when the incident THz wave is RCP, the corresponding Jones vector can be described as $\boldsymbol{E}_{\text{in}}=\sqrt{2}/2[1\ -\text{i}]^{\text{T}}$, and the electric vector of the transmitted THz wave is:

$$\boldsymbol{E}_{\text{out}}=\boldsymbol{J}\cdot E_{\text{in}}=-\frac{\sqrt{2}}{2}t_{xy}\text{e}^{\text{i}\varphi_{xy}(\alpha)}\cdot\text{e}^{\text{i}\theta}\begin{bmatrix}\cos\theta\\ \sin\theta\end{bmatrix}. \quad (5)$$

As evident from the above equation, the polarization state of the transmitted THz wave is determined by the angle θ of the bottom layer metagratings. Simultaneously, metagratings with different angles in different regions will introduce different θ phase factors, which require a $-\theta$ phase compensation.

To achieve nonlinear longitudinal polarization variations, the input phase plane is segmented into three regions. The transmitted wave in the innermost and outermost regions are pure E_x and E_y polarized, while the middle region is RCP, as shown in Fig. 2(e). To realize the RCP within the middle region, we combined 5×5 pixels into a larger unit and arranged a checkerboard pattern, filling them with 0° and 90° metagratings on the bottom layer. Due to the transmitted THz wave introducing a phase factor θ, a phase difference of π/2 is introduced into the complex amplitude of E_x and E_y within the middle region. In addition, the phase compensation corresponding to $-\theta$ is performed on the innermost and outermost region, respectively. Ultimately, this methodology facilitated the transition from linear to RCP and back to linear polarization along the predefined transmission trajectory. The corresponding polarization states at different propagation distances z are visualized on the Poincaré sphere, as illustrated in Fig. 2(f).

To achieve these special light fields, both polarization and phase modulation are required. Previous studies have achieved polarization manipulation of beam propagation trajectories using single-layer dielectric metasurfaces[34,38]. However, it is challenging to fabricate dielectric metasurfaces in the THz band due to the large wavelength of THz waves. On the other hand, a bilayer diatomic metasurface has been designed based on the detour phase method for vectorial holography in the visible light range[43]. However, the biatomic metasurfaces is limited to first-order diffraction, which poses a barrier to measurements in the THz band. Additionally, the dispersion caused by the different diffraction angles at different wavelengths will bring difficulties to broadband applications. Furthermore, the detour phase method requires a large pixel size which reduces the resolution of metasurface. Here, we use tri-layer metallic metasurfaces to achieve joint control of phase and polarization in the THz band. The schematic diagram of the tri-layer metallic metasurface unit structure is illustrated in Fig. 3(a). The unit cell comprises three layers of metallic structures separated by interlayer dielectrics, fabricated on a 500 μm thick high-resistance silicon substrate. The top and bottom layers consist of mutually orthogonal metagratings, while the middle layer comprises a C-shaped split-ring metallic structure. The metagratings are employed for polarization filtering, whereas the C-shaped split-ring is utilized for modulating the phase of the incident wave. Here we have performed 128-order quantization on the C-shaped split-ring antenna, and their phase delay covers 0–2π. Between the metal layers is the dielectric material polyimide (PI). At the same time, these layers form a Fabry-Perot like resonant cavity achieving a high operating efficiency over 75% in the transmission mode. The commercial software FDTD solutions was used to simulate the metasurface and optimize the parameters. The specific parameters are as follows: the operating frequency is 0.75 THz, and the unit period size is 100 μm. The thicknesses of the two PI layers and three metal layer structures are 40 μm and 150 nm, respectively. The width and period of the top and bottom metagratings are 10 μm and 20 μm, while the inner and outer diameters of the metal C-shaped split-ring antenna are 35 μm and 45 μm, respectively.

Results and discussion

A THz focal plane imaging system[44] was used to characterize the performance of the samples. The experimental set-up is shown in Fig. 4. A 35-fs ultra-short laser pulse with a central wavelength of 800 nm, a repetition rate of 1 kHz, and an average power of 900 mW was emitted from a Ti:sapphire regenerative amplifier. This laser pulse was split into two beams and employed as the pump and probe beams for generation and detection of THz waves. A ZnTe crystal with crystal orientation <110> was used to generate THz pulses through the optical rectification effect, while another ZnTe crystal with the same crystal orientation for detection. The THz complex field was extracted using balanced electro-optic detection.

Initially, along the proposed spatial structured light beam, we achieved a continuous linear polarization transition from 15° to 75° within the transmission range of z from 5 mm to 15 mm. The incident polarization

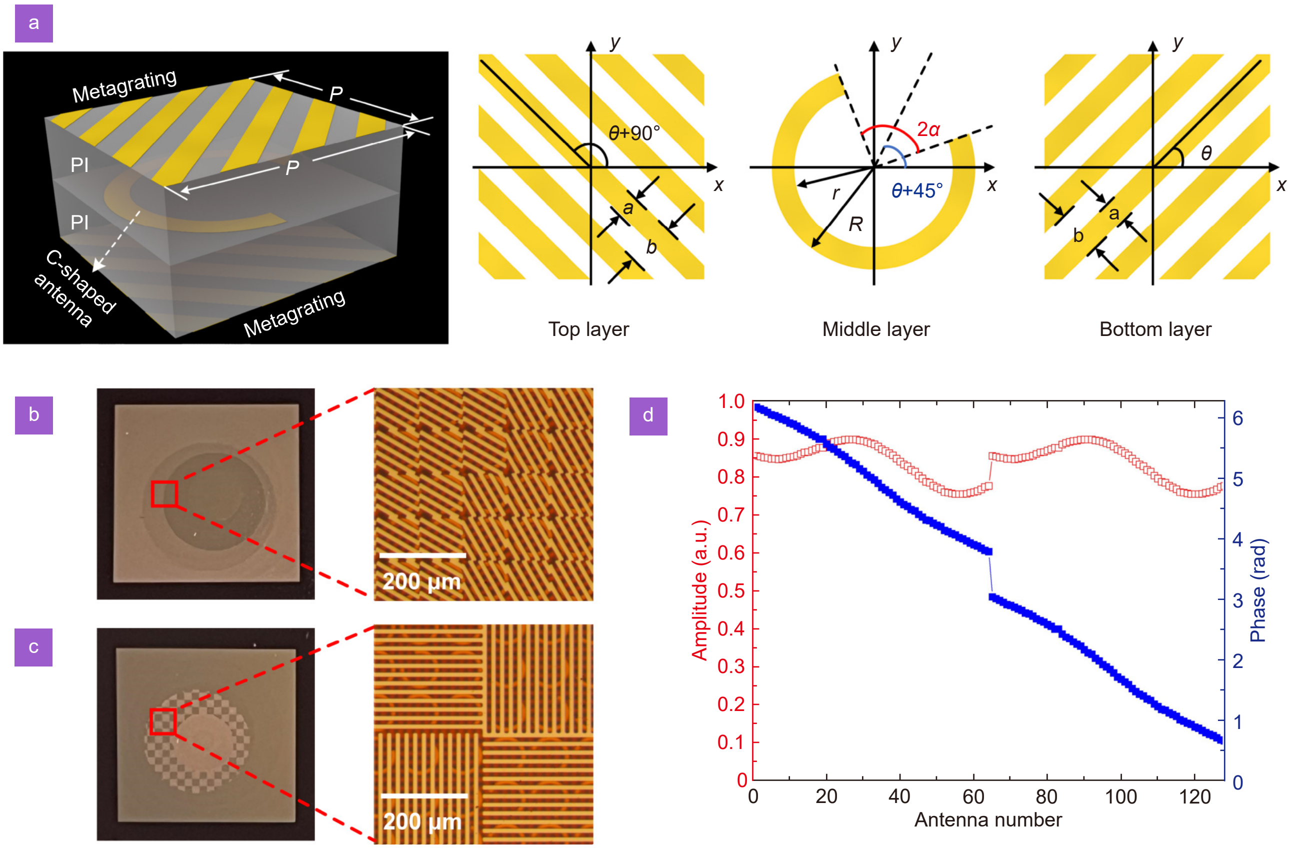

Fig. 3 | Schematic and characteristics of the designed unit cell. (**a**) Concept of the designed tri-layer metasurface and the metallic structure of each layer. (**b**, **c**) Microscope images of fabricated sample 1 and sample 2, respectively. The scale bar is 200 μm. (**d**) Amplitude and phase modulation of the 128 selected antennas at 0.75 THz.

state of THz radiation is RCP. The properties of the sample were characterized using the THz focal-plane imaging system. In the experiment, the complex fileds (including amplitude and phase information) for two orthogonal polarizations (x and y polarization) are measured, thus the intensity distributions on the cross-sections can be obtained, the point with maximum intensity can be found and the corresponding polarization on this point can be calculated. By manipulating the translation stage which carries the sample, the electric field distribution at different propagation distances z can be measured. Figure 5(a) and 5(b) depict the cross-sectional intensity profiles of the electric field at a propagation distance of z=15 mm for the simulation and experiment, respectively. Figure 5(c) presents the cross-sectional intensity profiles (red and blue solid lines) extracted from Fig. 5(a) and 5(b) along the white dashed lines. Modulated by the metasurface, the initial Gaussian beam exhibits a prominent bright central lobe surrounded by sidelobes. The distribution of the electric field intensity bears resemblance to a Bessel function pattern. The first and second rows of Fig. 5(d) display the intensity distributions at different distances for E_x and E_y components, respectively. From the experimental results, it is observed that the intensity I_x for the electric field component E_x reaches its maximum value when the transmission distance z=9 mm, subsequently, it gradually decreases with propagation distance enlarging, and becomes exceedingly weak when the transmission distance z=15 mm. Conversely, the intensity I_y of the electric field component E_y is very weak when the transmission distance z=5 mm, it gradually increases with the propagation distance increases. Simultaneously, to observe the cross-sectional distribution of the total electric field intensity I at different distances, the total intensity distributions I of the electric field at different distance are calculated and shown in the third row of Fig. 5(d). The distance is varied from 5 mm to 15 mm. The central bright spot is delineated by a white dashed line. It is observed that the intensity maximum point of the light spot moves during propagation. The trajectory closely follows the predefined circular helical path at sectional positions from z=5 mm to z=15 mm. Utilizing the measured amplitudes and phases of E_x and E_y, we synthesized the

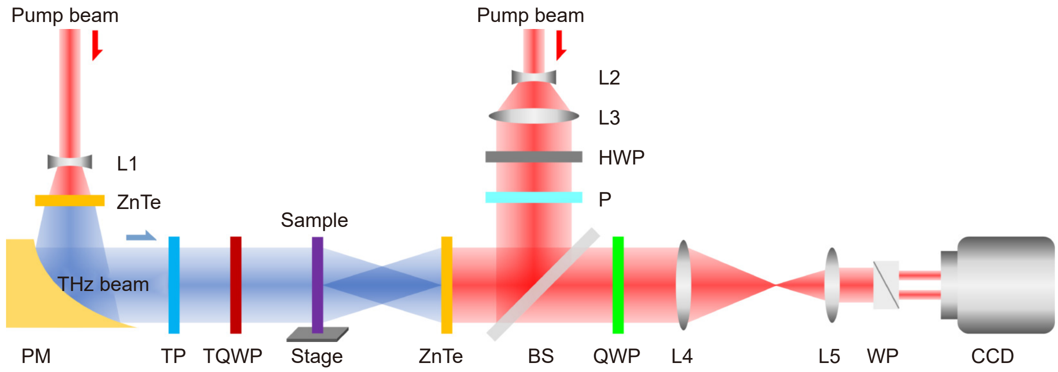

Fig. 4 | Schematic of experimental setup. L, lens; PM, parabolic mirror; TP, THz polarizer; TQWP, THz quarter wave plate; BS, beam splitter; HWP, half-wave-plate; P, polarizer, QWP; quarter wave plate; WP, Wollaston prism; CCD: charge-coupled device.

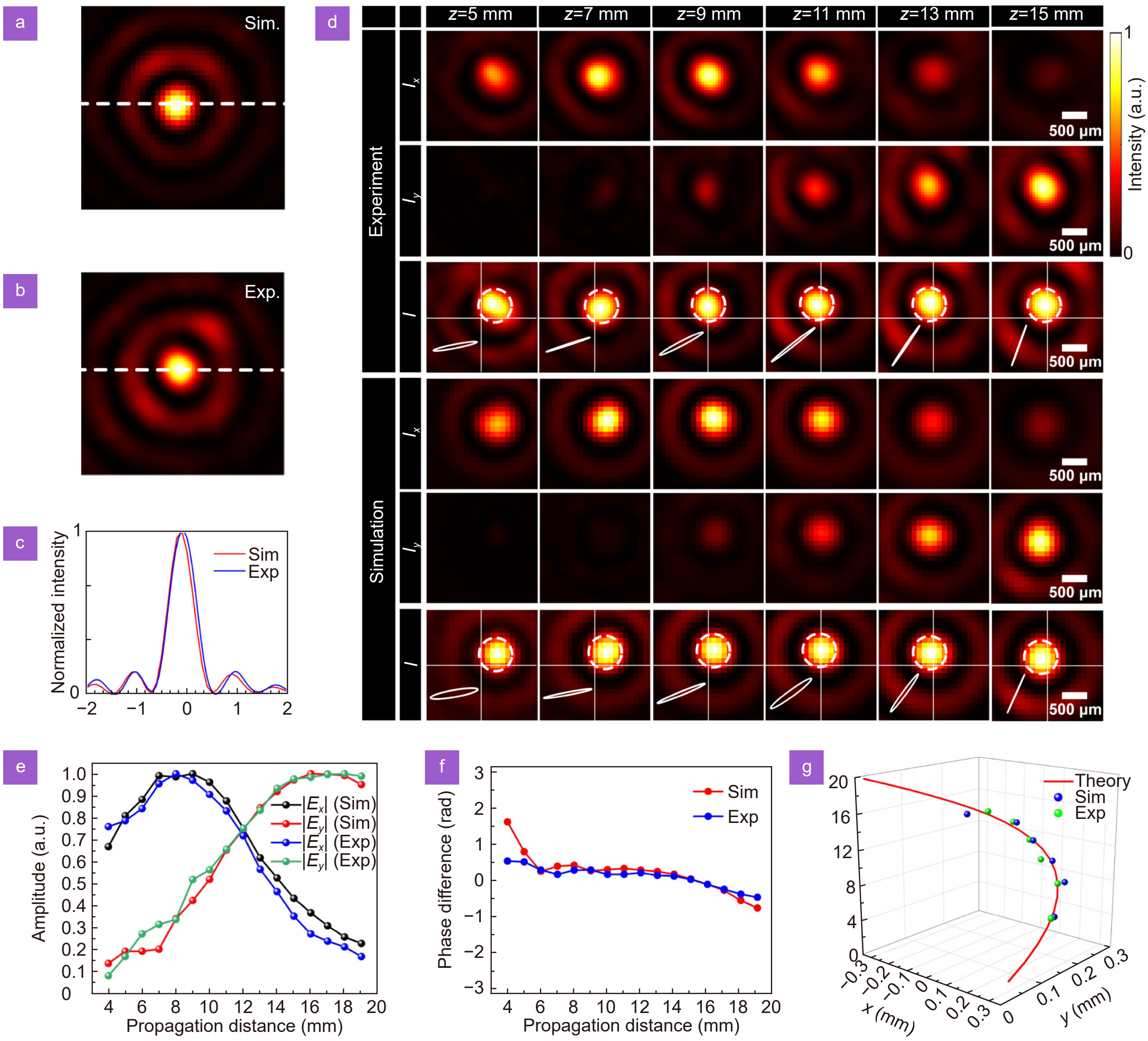

Fig. 5 | Experimental results for a structured light beam with linear longitudinal polarization variations along a helical transmission trajectory. (**a**, **b**) Cross-sectional intensity profiles of the electric field at a propagation distance of z=15 mm for the simulation and experiment, respectively. (**c**) Cross-sectional intensity profiles (red and blue solid lines) extracted from (a) and (b) at the locations of white dashed lines. (**d**) The electric field component intensity and electric field intensity at different distances. (**e**, **f**) Amplitudes and phase difference of electric field components E_x and E_y at different propagation distances. (**g**) Theoretical, simulated and experimental transmission trajectories.

polarization states at different propagation distances, as depicted in the lower-left corner of the third row in Fig. 5(d). Within the range from z=5 mm to z=15 mm, a continuous transition from 15° linear polarization to 75° linear polarization was achieved. Figure 5(e) and 5(f) respectively represent the simulated and experimental results of the amplitudes and phase difference of electric field components E_x and E_y at different propagation distances. Figure 5(g) shows the theoretical, simulated and experimental transmission trajectories.

On the same cylindrical helical trajectory ($f(z)$ = 0.3cos(πz/20), $g(z)$ = 0.3sin(πz/20)), we can change the polarization of state from linear polarization to elliptical polarization, RCP, elliptical polarization, and back to linear polarization again within the range of z from 5 mm to 15 mm. Figure 6(a) presents the intensity distribution of each electric field component and total field at different distances. It can be observed that the intensity I_x of the E_x component reaches its maximum value at a transmission distance of z=7 mm and gradually decreases as the transmission progresses, becoming extremely weak at z=15 mm, as shown in the first row of Fig. 6(a). Conversely, the intensity I_y of the E_y component is extremely weak at z=5 mm and gradually increases with the transmission distance, as depicted in the second row of Fig. 6(a). The total electric field intensity I at different distances are synthesized and shown in the third row of Fig. 6(a), the distance is ranged from 5 mm to 15 mm. The central bright spot is encircled by a white dashed line. It can also be observed that the central bright spot shifts with propagation, closely following the predefined cylindrical helical trajectory in the range of z=5 mm to z=15 mm. Utilizing the measured amplitudes and phases of E_x and E_y components, the polarization states are synthesized at different propagation distances, as shown in the bottom left corner of the third row of Fig. 6(a), achieving a gradual transition from linear to RCP and then back to linear polarization within the range of 5 mm to 15 mm. Figure 6(b) displays the simulated results and experimental results for the amplitudes of E_x and E_y components at different propagation distances, while Fig. 6(c) illustrates the corresponding phase difference between E_y and E_x components at different propagation distances. Figure 6(d) shows the theoretical, simulated and experimental transmission trajectories. The working efficiency was derived as the amplitude integral of the transmitted wave divided by the amplitude integral of the incident RCP THz wave, which was 0.384 in the experiment. It can be found that the working efficiency is almost half that of the three-layer metasurface unit, which is attributed to the underlying meta-grating reflecting half of the electric field of the incident RCP THz wave.

From above two experimental results, it can be found that within the 10 mm range of 5 mm –15 mm, the experimental and simulation results for the amplitudes of E_x and E_y at different distances are basically consistent. Beyond this range, the phase difference will have a large deviation. The possible reasons why the deviation becomes larger beyond the range of 10 mm are as follows: In this experiment, the THz radiation is generated from a ZnTe crystal pumped with femtosecond laser. In order to get enough signal-noise-ration for the THz focal plane imaging system, the size of THz beam is limited to 1.5 cm×1.5 cm, therefore, the size of sample is limited within 1.2 cm×1.2 cm. Since the size of a single pixel is 0.1 mm×0.1 mm, we have only 120×120 pixels to control the property of the generated structured light beam. Under these limitations, the final effective modulation range is about 10 mm. We believe that a larger THz spot and spatial bandwidth product can achieve more precise modulation over a longer range. In addition, it can be found that there is a large deviation between the simulation and experimental results at the end of the effective modulation range. This may be caused by the limitation of the THz spot size, alignment error of optical element, and fabrication error of metasurface.

Conclusion

In conclusion, we have put forth a new technique for creating spatially structured light beams in which the polarization continually and longitudinally varies along any transmission path. We have successfully shown two spatially structured light beams based on tri-layer metallic metasurfaces. Along a same helical transmission trajectory, one shows continuous variation in polarization states from 15° linear polarization to 75° linear polarization, while the other consistently transitions from 15° linear polarization to RCP and then back to 75° linear polarization. Our suggested approach, in our opinion, can offer a fresh viewpoint on tailored structured beams and discover uses for them in fields including particle manipulation, optical encryption, and biological imaging.

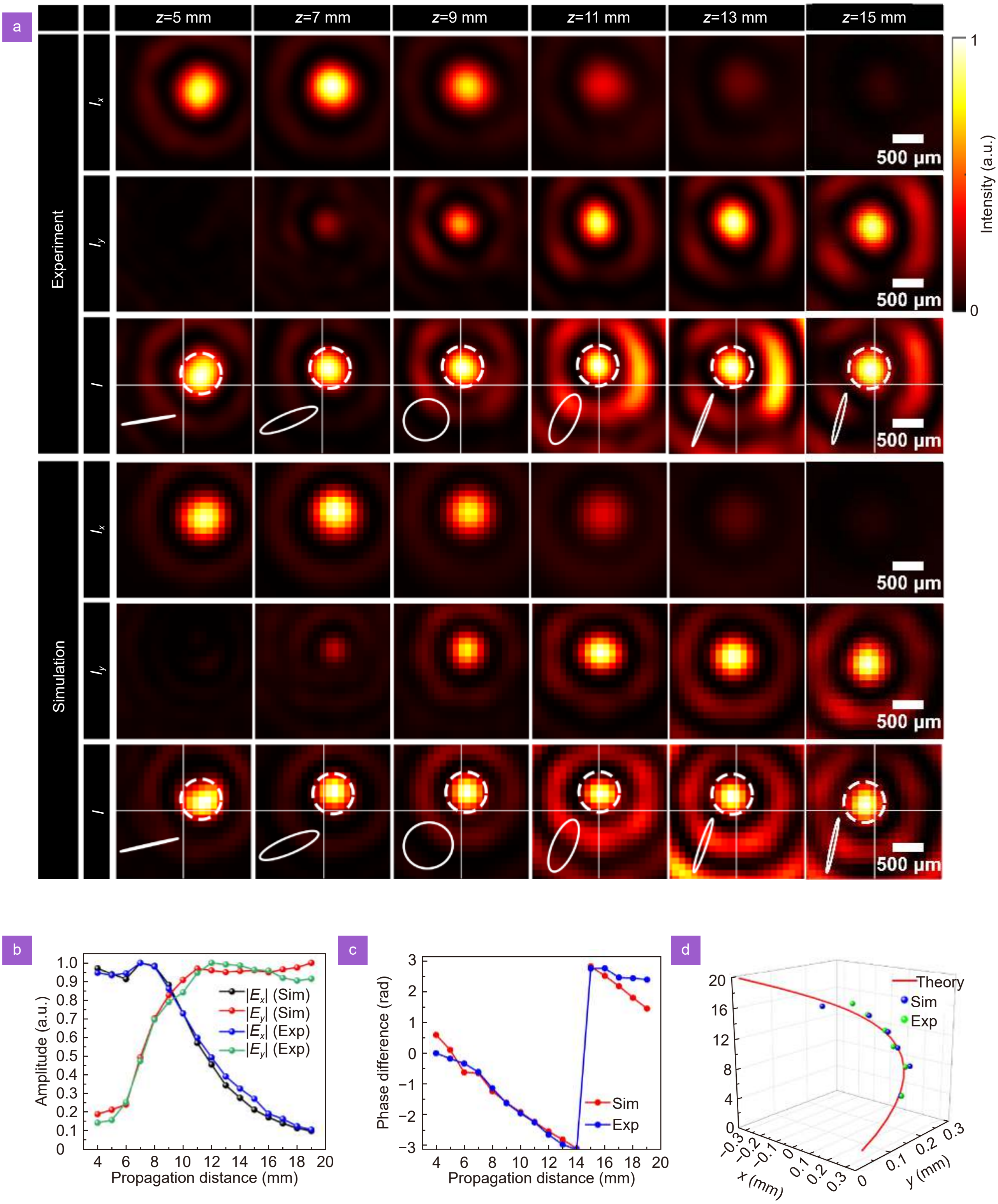

Fig. 6 | Experimental results of a structured light beam with nonlinear longitudinal polarization variations along a helical transmission trajectory. (**a**) Intensity distributions for E_x, E_y, and total electric field at different distances. (**b**) Simulated and experimental amplitudes and (**c**) phase difference of electric field components E_x and E_y at different propagation distances. (**d**) Theoretical, simulated and experimental transmission trajectories.

References

1. Forbes A, de Oliveira M, Dennis MR. Structured light. *Nat Photonics* **15**, 253–262 (2021).
2. He C, Shen YJ, Forbes A. Towards higher-dimensional structured light. *Light Sci Appl* **11**, 205 (2022).
3. Allen L, Beijersbergen MW, Spreeuw RJC et al. Orbital angular momentum of light and the transformation of Laguerre-Gaussian laser modes. *Phys Rev A* **45**, 8185–8189 (1992).
4. Durnin J, Miceli JJ Jr, Eberly JH. Diffraction-free beams. *Phys Rev Lett* **58**, 1499–1501 (1987).
5. Youngworth KS, Brown TG. Focusing of high numerical aperture cylindrical-vector beams. *Opt Express* **7**, 77–87 (2000).
6. Siviloglou GA, Christodoulides DN. Accelerating finite energy Airy beams. *Opt Lett* **32**, 979–981 (2007).
7. Chong A, Wan CH, Chen J et al. Generation of spatiotemporal optical vortices with controllable transverse orbital angular momentum. *Nat Photonics* **14**, 350–354 (2020).
8. Lu RW, Tanimoto M, Koyama M et al. 50 Hz volumetric functional imaging with continuously adjustable depth of focus. *Biomed Opt Express* **9**, 1964–1976 (2018).
9. Wang J, Yang JY, Fazal IM et al. Terabit free-space data transmission employing orbital angular momentum multiplexing. *Nat Photonics* **6**, 488–496 (2012).
10. Zhan QW, Leger JR. Microellipsometer with radial symmetry. *Appl Opt* **41**, 4630–4637 (2002).
11. Bozinovic N, Yue Y, Ren YX et al. Terabit-scale orbital angular momentum mode division multiplexing in fibers. *Science* **340**, 1545–1548 (2013).
12. Pu MB, Li X, Ma XL et al. Catenary optics for achromatic generation of perfect optical angular momentum. *Sci Adv* **1**, e1500396 (2015).
13. Padgett M, Bowman R. Tweezers with a twist. *Nat Photonics* **5**, 343–348 (2011).
14. He H, Friese MEJ, Heckenberg NR et al. Direct observation of transfer of angular momentum to absorptive particles from a laser beam with a phase singularity. *Phys Rev Lett* **75**, 826–829 (1995).
15. Zhang F, Guo YH, Pu MB et al. Meta-optics empowered vector visual cryptography for high security and rapid decryption. *Nat Commun* **14**, 1946 (2023).
16. Leach J, Jack B, Romero J et al. Quantum correlations in optical angle – orbital angular momentum variables. *Science* **329**, 662–665 (2010).
17. Zhang YW, Agnew M, Roger T et al. Simultaneous entanglement swapping of multiple orbital angular momentum states of light. *Nat Commun* **8**, 632 (2017).
18. Kozawa Y, Matsunaga D, Sato S. Superresolution imaging via superoscillation focusing of a radially polarized beam. *Optica* **5**, 86–92 (2018).
19. Yoshida M, Kozawa Y, Sato S. Subtraction imaging by the combination of higher-order vector beams for enhanced spatial resolution. *Opt Lett* **44**, 883–886 (2019).
20. Wang XL, Ding JP, Ni WJ et al. Generation of arbitrary vector beams with a spatial light modulator and a common path interferometric arrangement. *Opt Lett* **32**, 3549–3551 (2007).
21. Moreno I, Davis JA, Sánchez-López MM et al. Nondiffracting Bessel beams with polarization state that varies with propagation distance. *Opt Lett* **40**, 5451–5454 (2015).
22. Fu SY, Zhang SK, Gao CQ. Bessel beams with spatial oscillating polarization. *Sci Rep* **6**, 30765 (2016).
23. Guo JY, Wang XK, He JW et al. Generation of radial polarized Lorentz beam with single layer metasurface. *Adv Opt Mater* **6**, 1700925 (2018).
24. Buono WT, Forbes A. Nonlinear optics with structured light. *Opto-Electron Adv* **5**, 210174 (2022).
25. Zhao H, Wang XK, Quan BG et al. High-efficiency phase and polarization modulation metasurfaces. *Adv Photonics Res* **3**, 2100199 (2022).
26. Yu NF, Genevet P, Kats MA et al. Light propagation with phase discontinuities: generalized laws of reflection and refraction. *Science* **334**, 333–337 (2011).
27. He JW, Wang S, Xie ZW et al. Abruptly autofocusing terahertz waves with meta-hologram. *Opt Lett* **41**, 2787–2790 (2016).
28. Zhang YX, Pu MB, Jin JJ et al. Crosstalk-free achromatic full Stokes imaging polarimetry metasurface enabled by polarization-dependent phase optimization. *Opto-Electron Adv* **5**, 220058 (2022).
29. Wen J, Chen L, Yu BB et al. All-dielectric synthetic-phase metasurfaces generating practical airy beams. *ACS Nano* **15**, 1030–1038 (2021).
30. Wen J, Chen L, Chen X et al. Use of dielectric metasurfaces to generate deep-subwavelength nondiffractive Bessel-like beams with arbitrary trajectories and ultralarge deflection. *Laser Photon Rev* **15**, 2000487 (2021).
31. Zhao H, Wang XK, Liu ST et al. Highly efficient vectorial field manipulation using a transmitted tri-layer metasurface in the terahertz band. *Opto-Electron Adv* **6**, 220012 (2023).
32. Wang DY, Liu FF, Liu T et al. Efficient generation of complex vectorial optical fields with metasurfaces. *Light Sci Appl* **10**, 67 (2021).
33. Li TY, Li XY, Yan SH et al. Generation and conversion dynamics of dual Bessel beams with a photonic spin-dependent dielectric metasurface. *Phys Rev Appl* **15**, 014059 (2021).
34. Dorrah AH, Rubin NA, Zaidi A et al. Metasurface optics for on-demand polarization transformations along the optical path. *Nat Photonics* **15**, 287–296 (2021).
35. Li J, Liu J, Yue Z et al. Polarization variable terahertz metasurface along the propagation path. *Fundam Res*, (2023). https://doi.org/10.1016/j.fmre.2023.03.017
36. Zang XF, Ding HZ, Intaravanne Y et al. A multi-foci metalens with polarization-rotated focal points. *Laser Photon Rev* **13**, 1900182 (2019).
37. Li J, Li JT, Yue Z et al. Structured vector field manipulation of terahertz wave along the propagation direction based on dielectric metasurfaces. *Laser Photon Rev* **16**, 2200325 (2022).
38. Zhang F, Pu MB, Guo YH et al. Synthetic vector optical fields with spatial and temporal tunability. *Sci China Phys Mech Astron* **65**, 254211 (2022).
39. Zheng CL, Li J, Liu JY et al. Creating longitudinally varying vector vortex beams with an all‐dielectric metasurface. *Laser Photon Rev* **16**, 2200236 (2022).
40. Wang RX, Intaravanne Y, Li ST et al. Metalens for generating a customized vectorial focal curve. *Nano Lett* **21**, 2081–2087 (2021).
41. Chremmos ID, Chen ZG, Christodoulides DN et al. Bessel-like optical beams with arbitrary trajectories. *Optics Lett* **37**, 5003–5005 (2012).
42. Zhao JY, Zhang P, Deng DM et al. Observation of self-accelerating Bessel-like optical beams along arbitrary trajectories. *Op-*

tics Lett **38**, 498–500 (2013).

43. Deng ZL, Deng JH, Zhuang X et al. Diatomic metasurface for vectorial holography. *Nano Lett* **18**, 2885–2892 (2018).
44. Wang XK, Cui Y, Sun WF et al. Terahertz polarization real-time imaging based on balanced electro-optic detection. *J Opt Soc Am A* **27**, 2387–2393 (2010).

Acknowledgements

This work was supported by the National Natural Science Foundation of China (Grant Nos. 12074094 and 121774271), the Sino-German Mobility Program of the Sino-German Center for Science Funding (Grant No. M-0225), and the Capacity Building for Science & Technology Innovation-Fundamental Scientific Research Funds (Grant No. 00820531120017).

Competing interests

The authors declare no competing financial interests.

Supplementary information

Supplementary information for this paper is available at https://doi.org/10.29026/oes.2024.230052

Scan for Article PDF